44th AIAA Aerospace Sciences Meeting and Exhibit
9 - 12 January 2006, Reno, Nevada

AIAA 2006-1205

A Coupled Approach for Plasma-Based Flow Control Simulations of Wing Sections

Datta V. Gaitonde[*] & **Miguel R. Visbal**[†]
Computational Sciences Branch
Air Vehicles Directorate
Air Force Research Laboratory
Wright-Patterson AFB, OH 45433

Subrata Roy[‡]
Department of Mechanical Engineering
Kettering University
Flint, MI 48504

Numerical experiments in two- and three-dimensions, performed with a high-fidelity algorithm, are employed to explore plasma-actuator-based control of flow past a stalled NACA 0015 wing section. The time-accurate force field from a self-consistent asymmetric-electrode arrangement at $5kHz$ (continuous wave) is coupled to the Navier-Stokes equations at a nominal Reynolds number of $45,000$ and angle-of-attack of 15^o. When the actuator is placed slightly downstream of the separation point, the mean and asymptotic flow response include formation of a wall-jet and inhibition of separation. Features of the unsteadiness directly associated with the forcing, as well as that due to shedding occurring near the trailing edge are delineated. The results suggest that both streamwise and normal (towards the wall) components of force play important roles. A simpler phenomenological model is also employed to examine flow control in the full 3-D setting. At higher Reynolds number, $90,000$, the flow becomes turbulent immediately downstream of the leading edge and remains attached in the mean. The effect of the actuator in this situation is to laminarize the flow together with the formation of a wall-jet. When the actuator location is moved to the point of maximum thickness, laminar separation is induced near the leading edge with subsequent breakdown to turbulence. When stall is observed, at 18 deg angle of attack, placing the actuator near the leading edge yields the anticipated laminar wall jet on the upper surface. The effect of actuator force strength on separation suppression is examined in terms of the combined effect of transition to turbulence and near wall momentum enhancement. Finally, the effect of pulsing is documented at Reynolds number $45,000$ with 20% duty cycle and interpulse periods of 0.7 and 0.25 characteristic times respectively.

I. Introduction

Plasma-based techniques exploiting electromagnetic forces for flow control are currently of considerable interest. Particularly attractive properties are the absence of moving parts and lack of mechanical inertia, the latter facilitating near instantaneous deployment over a broad range of frequencies. Recent efforts have explored many possibilities both in high-speed as well as low-speed applications. The focus of this paper is on the latter speed regime, where striking experimental observations have been obtained at atmospheric pressures with glow discharges[1] or dielectric barrier discharge (DBD) based devices[2] operating in the low radio frequency range of $1 - 10kHz$ and voltage amplitudes of $5 - 10kV$. References 3–9 include some recent observations on separation control over various airfoil and turbine sections under static and oscillating conditions. An overview of some basic concepts behind this control technique, including impact of duty cycle, may be found in Ref. 10.

Despite this recent progress, a clear understanding of the physics of operation is presently lacking. A framework for analysis was proposed in Ref. 2 by associating the phenomenology to the characteristics of the DBD, thus bringing to bear kinetic theories developed in plasma physics disciplines in non-aerospace contexts. Further diagnostic efforts have been reported in Ref. 11, which, based on acoustic measurements, concluded that compressibility effects may play a role in momentum coupling, though as noted in Ref. 10 there is no significant heating of the air.

Numerical modeling of high-Reynolds number flows with purely first-principles based approaches is a daunting endeavor because quantitative aspects of many of the fundamental processes remain either unknown or cannot be

---

[*] Tech. Area Leader, High-Speed Flows Group, Associate Fellow AIAA
[†] Tech. Area Leader, Multi-Disciplinary Flows Group, Associate Fellow AIAA
[‡] Associate Professor, Associate Fellow AIAA.

resolved for the parameters of interest because of computational complexity. especially for air Additionally, situations in which flow control is essential, such as stalled airfoils, are characterized by flow transition to turbulence, which require massive simulation resources even without control. These difficulties have fostered the development of a wide spectrum of models introducing varying degrees of empirical elements into the procedure. Among the simpler methods focused specifically on discharge-fluid coupling, are those of Roth[12] and Shyy *et al.*[13] Roth associated transfer of momentum from charged to neutral particles as effectively based on a gradient of electric pressure, which varies as the square of the electric field magnitude. A more sophisticated model, suitable for coupling with the fluid response was proposed by Shyy *et al*,[13] who specify a spatially variable force field suited for coupling to high-fidelity numerical procedures. Other efforts include those of Corke *et al*[4] where the wall-jet characteristics are described and compared with experiment and of Voikhov *et al*,[14] who describe several 2-D simulations with a consistent approach satisfying Gauss' law.

The quest for more sophisticated tools utilizing plasma kinetic processes for first-principles simulations is being pursued on several fronts. The problem requires self-consistent solution of multi-dimensional multi-fluid equations, which implicitly couple the Maxwell and Navier-Stokes equations and incorporate various inter-molecular and electronic phenomena. Recent efforts with varying levels of sophistication are reported in Refs. 15–18. Of interest in the present paper is the procedure developed by Roy *et al* initially for 1-D phenomena[19] with subsequent extensions to 2-D configurations.[20,21] In a recent effort, Ref. 22, parametric studies are described examining the effect of amplitude and shape of excitation, dielectric constants, initial ionization level, electrode shape and sequential ganging of actuators. Key attributes of the method are simultaneous treatment of events in both the fluid as well as the dielectric, an integrated approach to coupling the Poisson equation and innovative methods of specifying boundary conditions.

In the present paper, the numerical effort initiated in Ref. 23 to examine flow control past a stalled NACA 0015 wing section at a nominal Reynolds number of $45,000$ and angle-of-attack $\alpha_a = 15^o$ (see Fig. 1a) is extended in several different respects. First, the response of the flow to spatially and temporally varying force field obtained from a first-principles simulation[21,22] is examined by direct coupling to the 2-D Navier-Stokes equations. The mean response is qualitatively compared to that obtained from a previously developed phenomenological model of the average force field. The relative impact of the negative voltage phase of the RF cycle is evaluated by damping the force during this time interval. In order to examine the effect of Reynolds number, angle of attack and force magnitude scaling, a 3-D approach is followed with a simplified force model. Finally, the effect of pulsing the force is also explored by fixing the duty cycle at 20% at two different interpulse periods of 0.7 and 0.25 T_c respectively, where T_c is the characteristic time.

II. Governing equations

The Navier-Stokes equations are solved with body force terms. In strong-conservation flux vector form and general curvilinear coordinates $x = x(\xi, \eta, \zeta)$, $y = y(\xi, \eta, \zeta)$, $z = z(\xi, \eta, \zeta)$:

$$\frac{\partial \hat{X}}{\partial t} + \frac{\partial \hat{F}_I}{\partial \xi} + \frac{\partial \hat{G}_I}{\partial \eta} + \frac{\partial \hat{H}_I}{\partial \zeta} = \frac{\partial \hat{F}_V}{\partial \xi} + \frac{\partial \hat{G}_V}{\partial \eta} + \frac{\partial \hat{H}_V}{\partial \zeta} + \hat{S} \tag{1}$$

where, $\hat{X} = \{\rho,\ \rho u,\ \rho v,\ \rho w,\ \rho e\}/J$ is the solution vector, J is the transformation Jacobian and $\hat{F}$, $\hat{G}$ and $\hat{H}$ are the flux vectors (subscripts I and V refer to inviscid and viscous components respectively). All quantities are non-dimensionalized with reference values, length c (chord), velocity $U_{ref} = U_\infty$, density $\rho_{ref} = \rho_\infty$ and temperature T_∞. In terms of the Cartesian fluxes,

$$\hat{F}_I = \frac{1}{J}(\xi_x F_I + \xi_y G_I + \xi_z H_I) \qquad \hat{F}_V = \frac{1}{J}(\xi_x F_V + \xi_y G_V + \xi_z H_V) \tag{2}$$

with similar expressions for the remaining flux vectors. For example, F_I, F_V and S are:

$$F_I = \left\{ \begin{array}{c} \rho u \\ \rho u^2 + p \\ \rho u v \\ \rho u w \\ (\rho e + p)\, u \end{array} \right\} F_V = \left\{ \begin{array}{c} 0 \\ \frac{1}{Re}\tau_{xx} \\ \frac{1}{Re}\tau_{xy} \\ \frac{1}{Re}\tau_{xz} \\ \frac{1}{Re}\left(u\tau_{xx} + v\tau_{xy} + w\tau_{xz}\right) + \frac{1}{(\gamma-1)PrM^2Re}\frac{\partial T}{\partial x} \end{array} \right\} S = \left\{ \begin{array}{c} 0 \\ D_c\rho_c e_c E_x \\ D_c\rho_c e_c E_x \\ D_c\rho_c e_c E_x \\ D_c\beta\rho_c(uE_x + vE_y + wE_z) \end{array} \right\} \tag{3}$$

where the Reynolds number is Re, Pr is the Prandtl number and M is the Mach number. $\hat{S} = S/J$, is the source vector containing the body force terms due to the plasma actuator. e_c is the electronic charge and the parameter D_c represents the scaling of the electrical to inertial forces:

$$D_c = \frac{\rho_{c,ref} e_c E_{ref} L_{ref}}{\rho_{ref} U_{ref}^2} \tag{4}$$

Details of the charge number density, ρ_c and electric field vector $\vec{E} = \{E_x, E_y, E_z\}$ are derived from models incorporating various degrees of phenomenological and first-principles components. In this work, both approaches are employed as described below, the former in 2-D to examine the effect of the high-frequency forcing on the flow and the latter in direct numerical simulations (3-D) to examine effect with variation of flow parameters (Reynolds number and angle-of-attack) and force pulsing.

III. Numerical Details

All simulations are performed at a very low Mach number of 0.1. Both 2-D and 3-D flows are simulated, the former for computationally intensive coupling with the first-principles unsteady force and the latter to examine the breakdown process with a phenomenologically modeled force. For the 3-D case, the spanwise extent of the domain is taken to be $0.2c$, where c is the chord length. A O-type mesh is employed, comprised of $308 \times 75 \times 145$ points in the x (streamwise), y (spanwise) and z (body-normal) directions respectively. The grid is generated by stacking planes in the manner shown in Fig. 1b. A view of each section is shown in Fig.1c, with an enlarged view in Fig. 1d. The mesh is stretched rapidly in the far-field towards the outer boundary, which is located $30c$ from the surface of the airfoil. The 2-D grid is generated by simply extracting a plane from the 3-D mesh. The boundary conditions are straightforward.

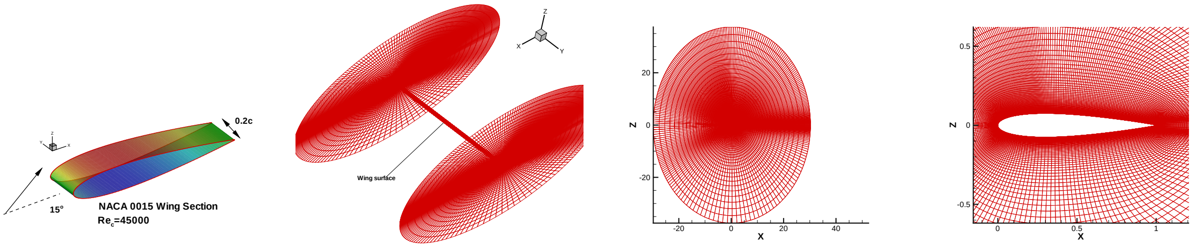

a) Problem simulated **b)** Overview of grid structure **c)** Sectional view **d)** Enlarged view

Figure 1. Grid structure

No-slip, zero body-normal pressure-gradient and isothermal wall conditions are enforced at the solid-wall. The far field is assumed to be far enough away for free-stream conditions to be valid while periodic conditions are applied in the spanwise direction as well as at the branch cut arising due to the O-type mesh.

A high-order compact-difference method is employed to solve the governing equations. Derivatives, ϕ', of each required quantity, ϕ, are obtained in the uniformly discretized transformed plane (ξ, η, ζ) with the formula:

$$\Gamma_s \phi'_{i-1} + \phi'_i + \Gamma_s \phi'_{i+1} = b_s \frac{\phi_{i+2} - \phi_{i-2}}{4} + a_s \frac{\phi_{i+1} - \phi_{i-1}}{2} \tag{5}$$

where Γ_s, a_s and b_s determine the spatial properties of the scheme. All simulations described in this work employ the sixth-order *C6* method, for which $\Gamma_s = 1/3$, $a_s = 14/9$ and $b_s = 1/9$. Details of the spectral characteristics of these schemes, and others obtainable from Eqn. 5, may be found in Refs. 24–26.

Additional components are required in the method to enforce numerical stability, which can be compromised by mesh stretching, boundary condition implementation and non-linear phenomena. Spurious frequencies in the solution are systematically removed with a filter designed using spectral analysis. For any component of the conserved vector, ϕ:

$$\alpha_f \hat{\phi}_{i-1} + \hat{\phi}_i + \alpha_f \hat{\phi}_{i+1} = \Sigma_{n=0}^{N} \frac{a_n}{2} \left(\phi_{i+n} + \phi_{i-n}\right) \tag{6}$$

where $\hat{\phi}$ is the filtered value. Relevant spectral analyses may be found in Ref. 27. In the present work, the $8th$ order filter with $\alpha_f = 0.2$ is employed in the body-normal and streamwise directions, while the $10th$ order filter with $\alpha_f = 0.4$ is chosen in the spanwise periodic direction.

IV. Results

The baseline flow has been described in a previous effort.[23] The key features are reproduced in Fig. 2 showing iso-levels of instantaneous vorticity magnitude colored by the spanwise component of vorticity (Fig. 2a) and instantaneous and mean velocity contours in the mid-span plane. The breakdown of the shear layer very shortly after separation is clearly evident, generating smaller structures and spanwise instabilities. Although the process is highly three-dimensional, and requires a direct numerical simulation for complete representation, in order to describe the flow succinctly, instantaneous quantities will be plotted at the mid-span plane. Figures 2b and c show the instantaneous u-velocity and the vorticity magnitude. The shear layer emanates from the separation point, which occurs at approximately 2% chord and the flow may be considered to be fully stalled. Proceeding downstream, the layer loses its coherence as the three-dimensional break-up process progresses. The flow beneath the shear layer is transitional, and is characterized by very low velocities. Reference 23 contains additional description of the no-control 3-D flow, pertinent aspects of which will be reiterated in the context of the new results below where warranted.

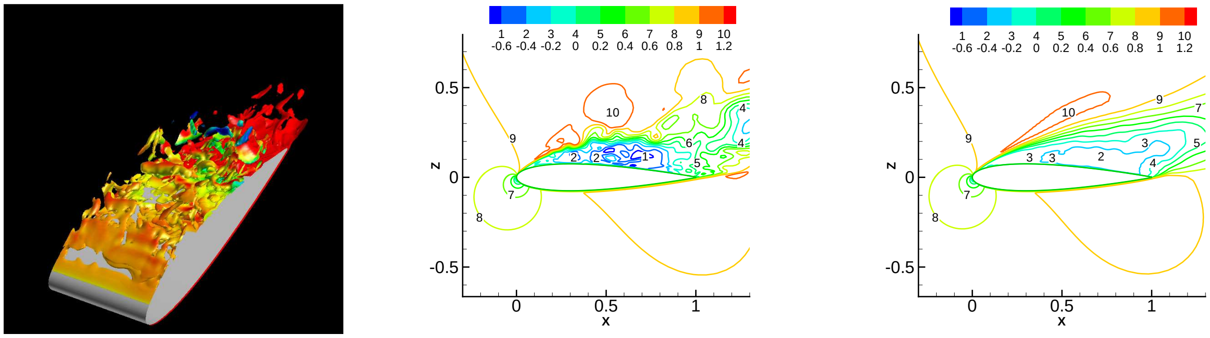

a) 3-D structure - isolevs **b)** instantaneous u-velocity (mid-span) **c)** mean u-velocity

Figure 2. Structure of 3-D flowfield without control

The two-dimensional baseline flow is rather different than in 3-D because of the absence of a spanwise breakdown mechanism. Contours of select instantaneous and mean quantities are plotted in Fig. 3. In this case, shed vortices maintain their coherence in an unphysical fashion, giving rise to a sequence of large vortex pair structures that are shed downstream. Peak instantaneous velocities, Fig. 3a, are considerably larger in localized regions, reaching almost twice those observed in the 3-D simulations. In a consistent fashion, instantaneous pressure contours exhibit coherent features in which extrema are much higher than in the full 3-D simulation. The mean u contours, Fig. 3c, shows significant qualitative and quantitative differences from both instantaneous 2-D and mean 3-D counterparts, with a lower incline of the separated shear layer relative to the surface of the airfoil.

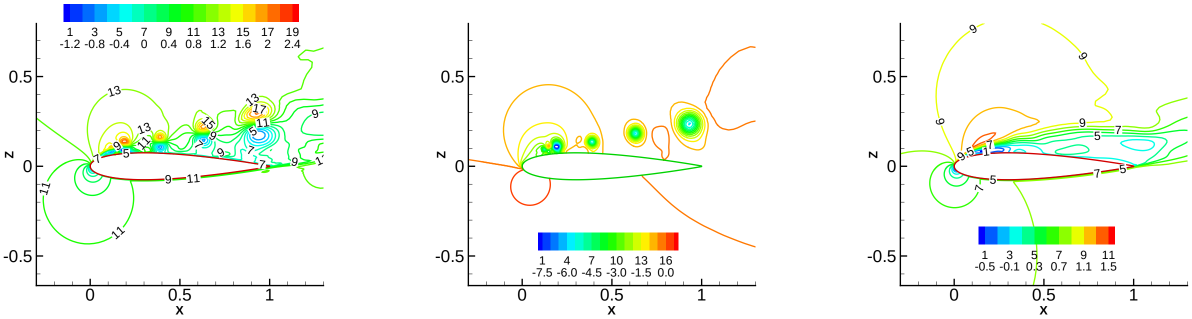

a) Instantaneous u velocity **b)** Instantaneous pressure **c)** Mean u velocity

Figure 3. Structure obtained with 2-D simulations without control

A. Coupling of force field obtained from first-principles approach

1. Time-varying nature of force field

The plasma effect is coupled to the Navier-Stokes equations through the body force, which depends on the net space charge and electric field distributions. The charge density, ρ_c and the electric field $\vec{E}$ are obtained in a self-consistent fashion following the procedure described in Ref. 21,22. Briefly, the two-dimensional three-species collisional plasma-sheath model includes the charge and momentum continuity equations, and Gauss' law for electric potential:

$$\frac{\partial n_\alpha}{\partial t} + \frac{\partial}{\partial x_j} n_\alpha V_{\alpha j} = n_e z - r n_e n_i \tag{7}$$

$$n_\alpha V_{\alpha j} = \text{sgn}(e) n_\alpha \mu_\alpha \frac{\partial \phi}{\partial x_j} - D_\alpha \frac{\partial n_\alpha}{\partial x_j} \tag{8}$$

$$\epsilon \left(\frac{\partial^2 \phi}{\partial x^2} \right) = e \left(n_e - n_i \right) \tag{9}$$

The charged particle subscript α refer to electrons, e or ions, i respectively, n is the number density, V_j the velocity vector and z and r are the ionization and recombination coefficients. Since air chemistry for the pertinent processes in the discharge remain poorly understood, several assumptions are made to obtain representative features of the time-varying force field. First, the distribution and variation of charge and electric field are obtained under the assumption that the working gas is helium and secondary emission is currently ignored. The scope of this effort is thus on developing the coupling framework and examining fluid response to a force fluctuating at kHz frequency. The effort to lift limitations in current thermo-chemical data for the environment of interest is being pursued separately. A degree of quantitative accuracy is reintroduced through empiricism by scaling the force to match peak amplitudes obtained from phenomenological considerations in Refs. 13, 23. The electron temperature is assumed to be uniform at $1eV$, while ions and neutrals are assumed to be in thermal equilibrium at $300K$. Electron diffusion is obtained from the Einstein relation while the ion diffusion coefficient, mobility, ionization and recombination rate coefficients, which are functions of the electric field magnitude and the pressure, and taken from the literature.[28]

The above equations are solved with the multiscale ionized gas (MIG) flow code, developed at the Computational Plasma Dynamics Laboratory at Kettering University. The method is based on a versatile finite-element (FE) procedure adapted from fluid dynamics to overcome the stiffness of the equations generated by multi-species charge separation phenomena. A 2D bilinear finite element formulation is chosen with 4th order Runge-Kutta time marching. The solution process consists of two steps. The first solves the equations for charge and electric field simultaneously. In the second step, the force so obtained is transferred to the airfoil after rotation and scaling and constitutes the source term in Eqn. 3, with $\rho_c = (n_i - n_e)$. The MIG code also solves for the self-consistent fluid response, which is not factored in the present analysis (see Ref. 22). This implicitly assumes that the near-wall local fluid neutral velocity does not influence the distribution of electric parameters. This requires that the fluid density and pressure, or collisionality, are not much different from those employed in the plasma calculation. This is a reasonable expectation for the low-speed atmospheric pressure incompressible flows of interest here. Further details may be found in Refs. 22, 29–31.

The equations are solved in the region surrounding a small flat surface which demarkates the ambient medium from the dielectric. The electrodes are placed in a staggered manner as shown in Fig. 4a, with the exposed electrode ($12mm$ long) being located upstream of the embedded electrode ($12.7mm$ long). The vertical distance between the electrodes is $1mm$ and a $0.2mm$ horizontal overlap exists between the two. The exposed electrode is excited at a signal of $5kHz$ and $2kV$ *rms* amplitude. The dielectric constant of the fluid is assumed to be $1.0055\epsilon_o$ while that of the solid is assumed to be $3.5\epsilon_o$, where ϵ_o refers to the property of free space. The mesh employed, shown in Fig. 4b, consists of 103×106 nodes, clustered near the electrodes in the vertical direction, and near electrode edges in the streamwise direction. The vertical height of the simulated domain extends $20mm$ above the surface and $1mm$ beneath it. Inside the dielectric, the only component of current is associated with the change of electric field displacement. At the interface, this value is matched with that associated with electron flow in the fluid towards the surface on which charge accumulation is allowed to occur. Details of the variation of electromagnetic fields at different phase angles are provided in Ref. 21. Charge, electric field and force vector distributions at the peak of the forward phase ($\phi = \pi/2$) are shown in Fig. 4 c and d respectively. The charge distribution consists of regions of net positive as well as negative ranges. At the instant shown, the negative charge is restricted to a very small region at the dielectric surface above the embedded electrode. In most regions away from the surface, the ion concentration is larger and the net charge is positive. Electric field vectors at the same instant, Fig. 4d, are consistent with the charge through Gauss' law. Large amplitudes are evident near the trailing edge of the exposed electrode. At the dielectric surface, the direction of the field changes relatively abruptly from upward (into the flow) to pointing downward. The magnitude diminishes rapidly in the x-direction, together with a reversal of direction. Thus upstream pointing vectors are evident aft of the exposed electrode. The body force field vectors are presented in Fig. 4e. Since the charge is positive in most regions at this phase angle, the force and electric field are generally similar. The mean force field is shown in Fig. 4f. In the crucial region near the trailing edge of the exposed electrode, the pattern is generally similar to that in Fig. 4e with

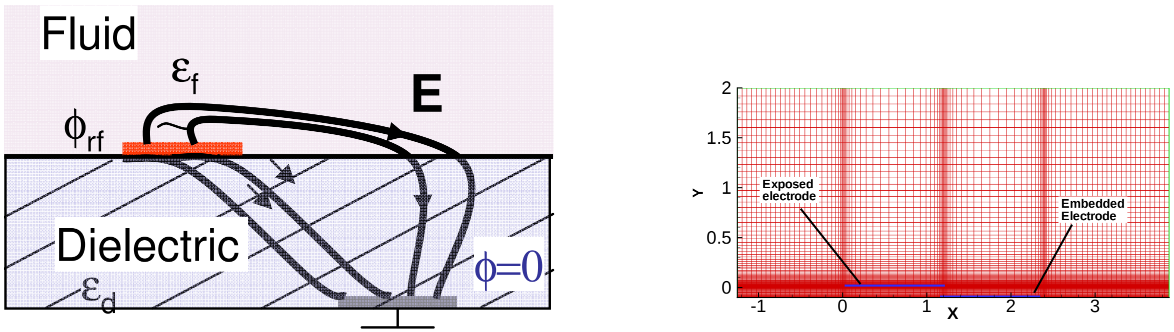

a) Schematic **b)** Mesh employed

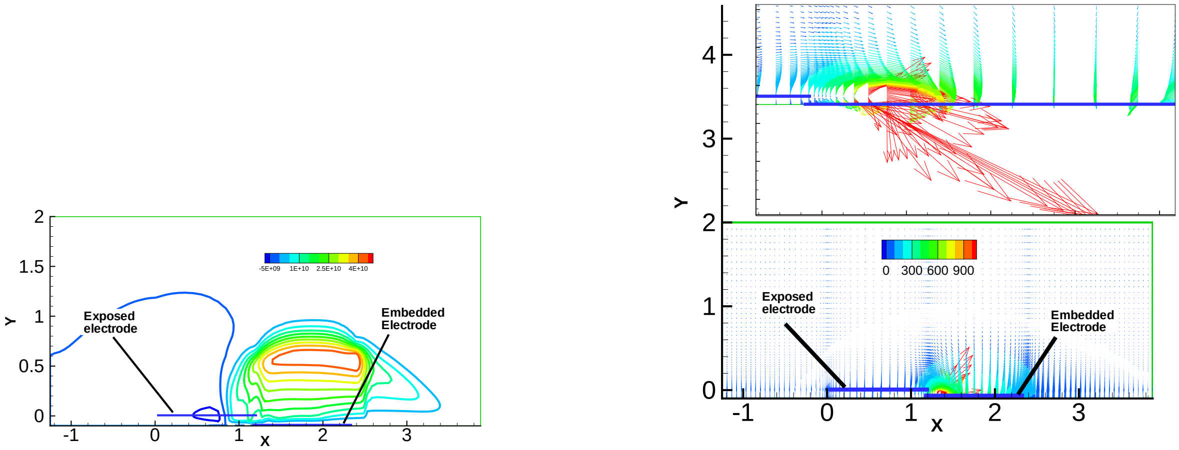

c) Charge at $\phi = \pi/2$ **d)** E-field at $\phi = \pi/2$

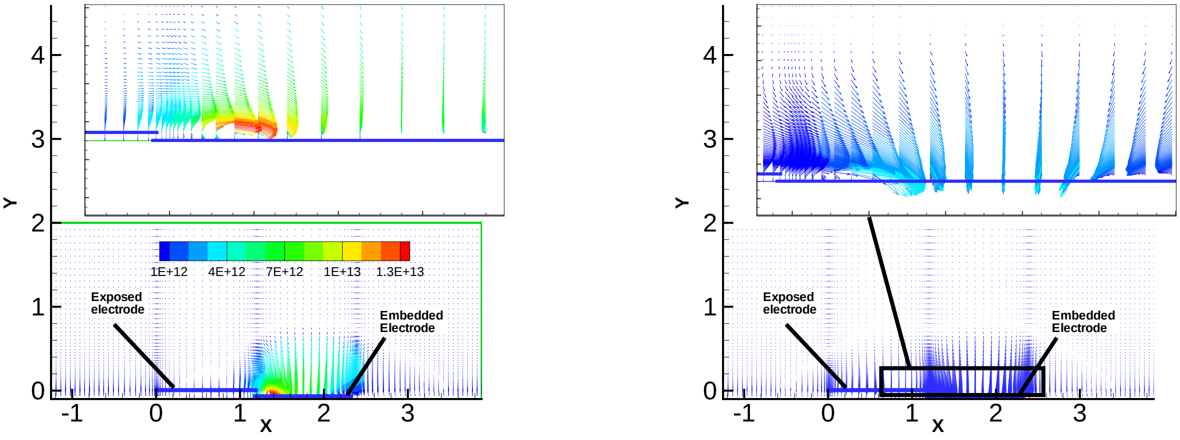

e) Force at $\phi = \pi/2$ **f)** Average Force

Figure 4. Features of self-consistent simulation of plasma actuator on flat plate configuration

a predominantly downward/streamwise orientation. In other regions, the force exhibits components away from the surface (over the exposed electrode), as well as towards it (above the dielectric). The impact of the difference between the variation of Fig. 4f and the phenomenological models of Refs. 13, 23, which assume a triangular region of force, is not presently known for all parameters. It will be shown later however, that for the cases explored in this study, the average response to the unsteady force bears great resemblence to that obtained with the phenomenological model, though quantitative differences exist for similarly scaled force fields.

The superposition of time-varying force on the airfoil mesh is shown Fig. 5 at several phase angles of the input signal. The manner in which this transformation was conducted is as follows. The downstream edge of the exposed electrode was mapped to a selected point on the airfoil. Unless otherwise stated, this point lies slightly downstream of separation ($X_o = x_o/c = 0.028, Z_o = z_o/c = 0.034$) observed at $Re = 45,000$, $\alpha_a = 15^o$. At this point, a local orthogonal coordinate system, $x' - z'$ is defined such that x' is tangent to the surface. The rectangular domain of Fig. 4b is mapped to this local system by simple rotation operations. The domain of active force is then scaled by a factor of 100 so that the length and height of the region are roughly 3% and 2% chord respectively, similar to that employed with the phenomenological model.[23] At each point on the airfoil grid, the force contribution is then computed through bilinear interpolation, with area-weighting to ensure matching of integrated force. This process is carried out for each phase angle and the force field on the airfoil is stored for subsequent use as below. The amplitude of the force is first normalized by peak value in the cycle - this greatly facilitates subsequent magnitude control through the coefficient D_c defined above. Following Ref. 23, the nominal value for D_c is 2400, which is obtained by assuming a charge density of $10^{11}/cm^3$, peak electric field magnitude of $226.27kV/cm$ (both taken from Ref. 13), chord lenth of $12.7cm$ and Reynolds number $45,000$ at atmospheric conditions.

At each time-instant in the Navier-Stokes simulation, the phase angle within a cycle is computed from knowledge of the period of the cycle, and the time at which the control was initiated. It is then a simple matter to linearly interpolate between known (stored) adjacent phase angles obtained from the above spatial and temporal integration process. In the cases described below, the non-dimensional time-step was fixed at 5×10^{-5}. Since the non-dimensional period of the $5kHz$ signal is $T_a = 4.7 \times 10^{-3}$, about 95 time-steps span a single cycle.

The force field variation over a cycle is shown in Fig. 5. In the "positive" segment, *i.e.*, where the input voltage is positive, the force field very near the surface at X_o, Z_o, is directed downward towards the reference point. Slightly downstream, the force has a significant streamwise component as well. Proceeding outwards from the wall, the force obtains an upward-downstream orientation. The amplitudes rise rapidly with time though a small lag is observed between magnitude and phase- note the relatively larger force field at $\phi = 6\pi/10$ compared to that at $\phi = 4\pi/10$ and the observation that the force field at $\phi = \pi$ is non-zero. On the "negative" stroke, the amplitude of the force is relatively smaller. The force is predominantly towards the surface, though significant upstream components are evident above the embedded electrode.

2. Response to time-varying force: unsteady flowfield

When the flow is subjected to the above body force, the response may be classified into an initial response during which the large separated region is eliminated, and an asymptotic periodic state. The initial response is shown in terms of u-velocity, pressure and spanwise-vorticity ω_y, in Fig. 6 - the flow time marked is relative to the onset of control. The initial frame, $T = 0.01T_c$ shows the typical structure observed in two-dimensional simulations of stall - the flow is characterized by large vortical structures that are convected downstream without breakdown because of the absence of a 3-D instability mechanisms in the 2-D simulation. The control technique suppresses the formation of new structures that ordinarily would have formed. The development of the apparent attachment is relatively monotonic, starting near the point of application of the body force and progressing downstream. The initial signal reaches the trailing edge at $T \sim 1.5T_c$, when the original large vortical structures have convected downstream of the wing section. The situation at an instant after several characteristic times have elapsed, , $T = 5.3T_c$, indicates an attached flow over most of the airfoil, though an unsteady shear layer is evident near the traililng edge. The acoustic impact of the actuator is most obvious near the point of application as observed in the pressure contours. Although the acoustic signal yields large relative fluctuations compared to the no-control case, its amplitude diminishes with distance, an effect which is enhanced by the coarser mesh resolution away from the surface. Further details of the unsteadiness observed in the pressure field are described below. Vorticity contours also demonstrate the convection of the initial structures, and, at asymptotic state indicate clearly the development of organized structures in the shear layer separating near the trailing edge. With this force magnitude, flow attachment is not complete in this sense. It should be noted, following the discussion in Ref. 23 and in the context of Fig. 3, that the evolution of naturally induced unsteady features such as these are not generally correctly reproduced in 2-D simulations because of the absence of a spanwise breakdown mechanism.

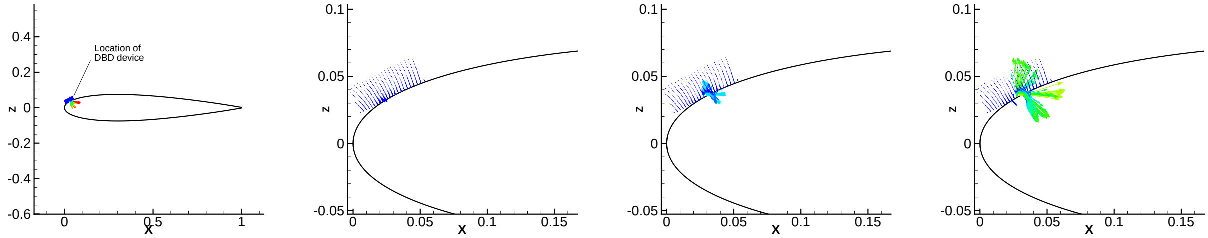

a) Overview **b)** Phase=0 **c)** Phase=$\pi/10$ **d)** Phase=$2\pi/10$

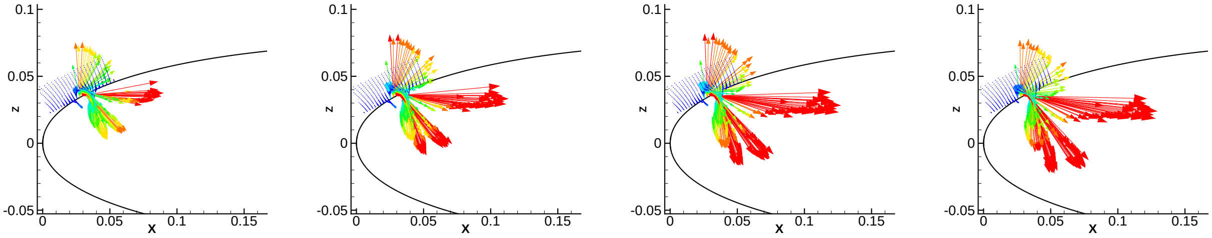

e) Phase=$3\pi/10$ **f)** Phase=$4\pi/10$ **g)** Phase=$5\pi/10$ **h)** Phase=$6\pi/10$

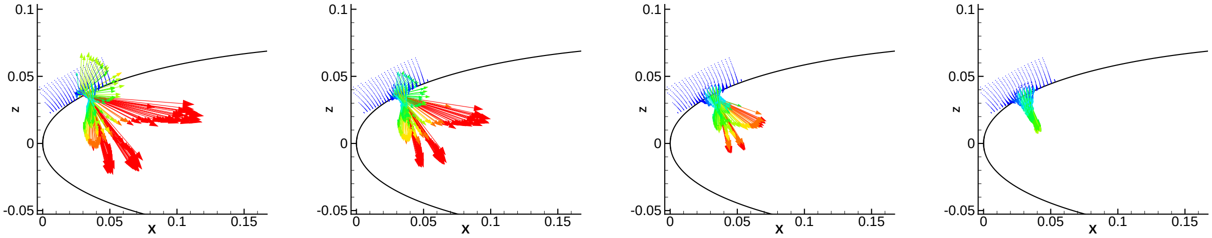

i) Phase=$7\pi/10$ **j)** Phase=$8\pi/10$ **k)** Phase=$9\pi/10$ **l)** Phase=$10\pi/10$

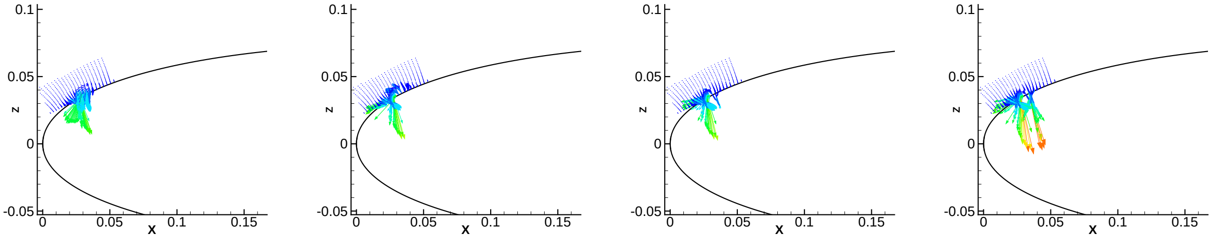

m) Phase=$11\pi/10$ **n)** Phase=$12\pi/10$ **o)** Phase=$13\pi/10$ **p)** Phase=$14\pi/10$

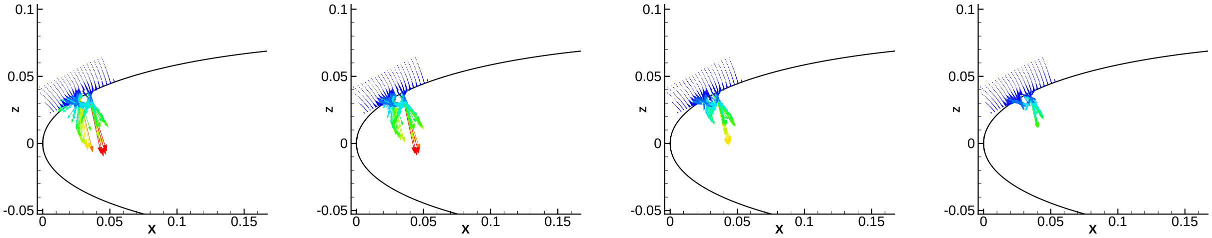

q) Phase=$15\pi/10$ **r)** Phase=$16\pi/10$ **s)** Phase=$17\pi/10$ **t)** Phase=$18\pi/10$

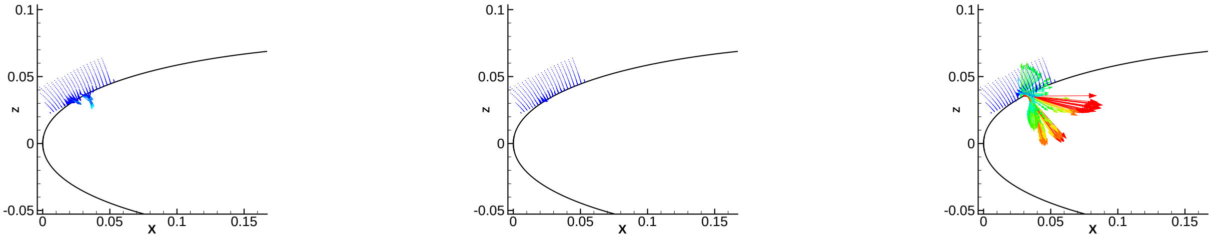

u) Phase=$19\pi/10$ **v)** Phase=$20\pi/10$ **w)** Average

Figure 5. Force field on airfoil at different phases in a single cycle of excitation after asymptotic state is reached

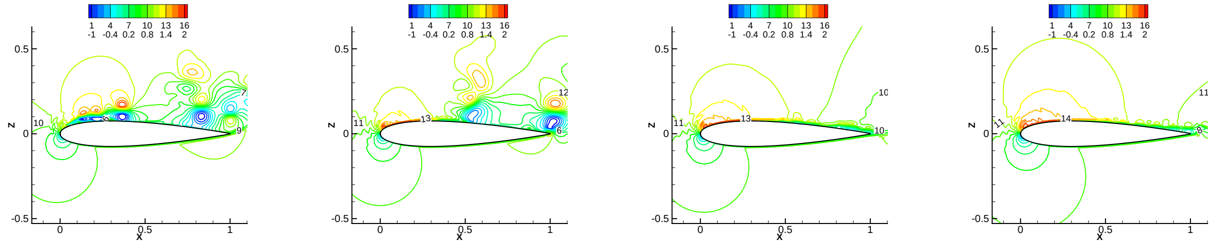

a) u at $T = 0.01T_c$ **b)** u at $T = 0.5T_c$ **c)** u at $T = 1.5T_c$ **d)** u at $T = 5.3T_c$

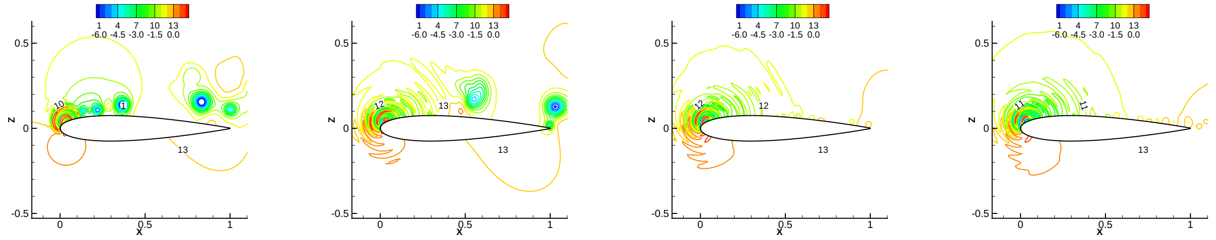

e) p at $T = 0.01T_c$ **f)** p at $T = 0.5T_c$ **g)** p at $T = 1.5T_c$ **h)** p at $T = 5.3T_c$

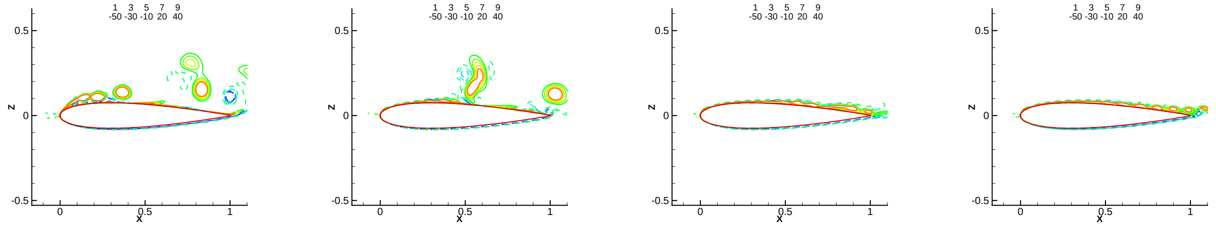

i) ω_y at $T = 0.01T_c$ **j)** ω_y at $T = 0.5T_c$ **k)** ω_y at $T = 1.5T_c$ **l)** ω_y at $T = 5.3T_c$

Figure 6. Initial transient and unsteady long term response with spatio-temporally varying force

The nature of the unsteadiness encountered within an individual cycle are described in Fig. 7. Surface static pressures at the leading edge, mid-chord and at the trailing edge are plotted in Fig 7a at intervals which are roughly 2 actuator periods apart. Large oscillations are evident near the leading edge, which, of the three stations plotted is closest to the actuator. The excursions from the mean diminish downstream. The fine scale nature of the signal is shown in Fig. 7b, where pressure is plotted at every computed time instant for several actuator excitation periods. The dominant frequency near the leading edge is evidently much higher than that observed downstream. Fourier analysis, Fig. 7c, indicates that near the leading edge, the primary frequency is that of the actuator, while the smaller values at the other locations are associated with shedding of large scale structures, described earlier. The response of velocity profiles in the field at several phase angles within one actuator cycle is exhibited in Fig. 7d. Three profiles are shown, just downstream of the actuator ($X = 0.11$), mid-chord ($X = 0.5$) and at the trailing edge ($X = 1$) respectively. Near the actuator, the existence of the wall jet like structure, with peak velocities of about $2.4U_\infty$, is prominent. Examination of the inset reveals that the peak velocity varies by about 4% within the cycle. At mid-chord, the fullness of the profile diminishes, the peak decreases to $1.5U_\infty$ while it location moves away from the wall. At the trailing edge, the velocity achieves negative values as the profile cuts across a coherent structure that develops near the trailing edge (see Fig. 6).

3. *Response to time-varying force: time-averaged flowfield*

Aspects of the flow field described above, averaged over several characteristic times after the asymptotic state is reached are shown in Fig.8. Close examination of the solution indicates that the point of separation point moves downstream relative to the no control case, but only to about $x/c = 0.4$, which is beyond the maximum thickness location. However, the reversed flow layer remains restricted to the near wall region for significant distance, and there is little displacement impact on the outer flow. Gross manifestations of separation, including shear layer detachment from the surface, become apparent only much further downstream, $x/c \sim 0.85$, similar to the experimental visualizations reported in Ref. 12. The mean pressure contours, Fig. 8b are characteristic of an attached flow, with acoustic signals noted earlier in the instantaneous contours having been averaged out. The development of the wall-jet yields a reversal of sign of the sole vorticity component (ω_y) pointing out of the plane of the figure.

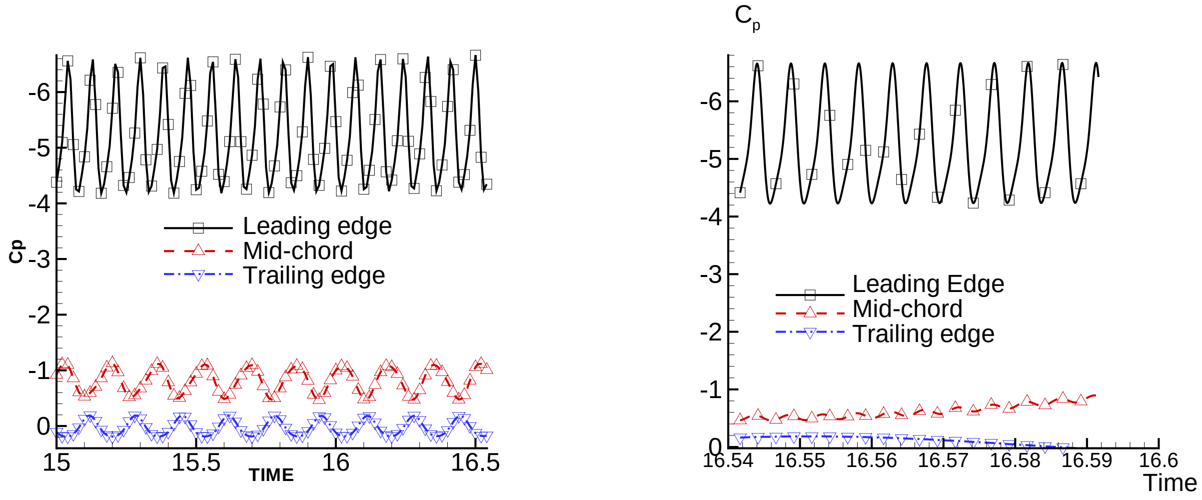

a) Surface pressure sampled $2T_a$ apart

b) Surface pressure sampled at each time-step

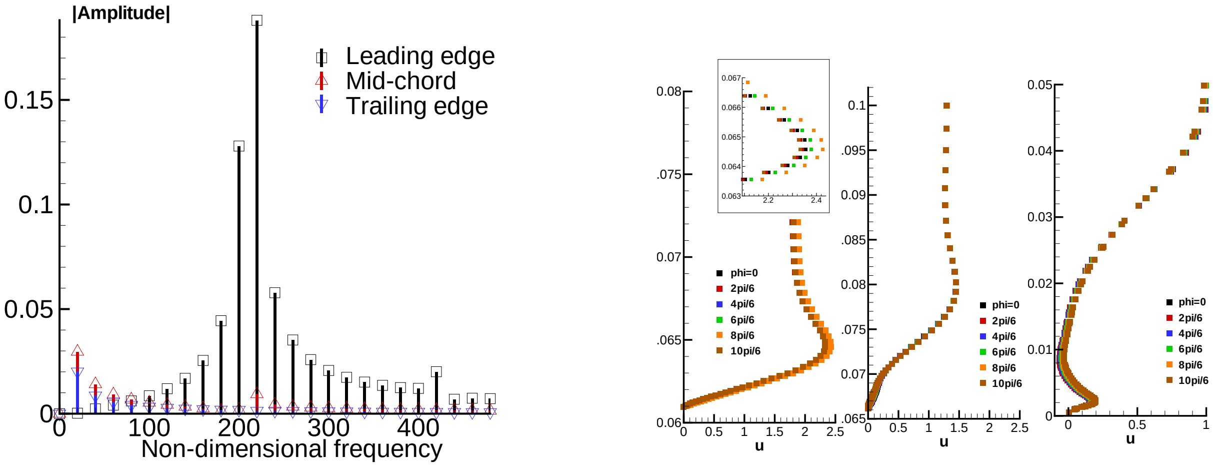

c) FFT analysis

d) Velocity profiles

Figure 7. Aspects of unsteady response to time-varying body force field

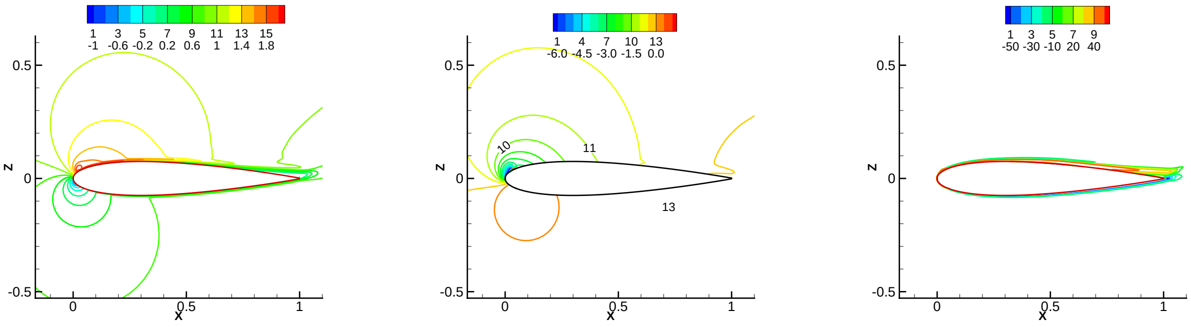

a) u

b) C_p

c) ω_y

Figure 8. Mean response of flow field to time-varying force

4. *Response to steady averaged force*

Phenomenological models, such as those described in Refs. 13, 23 employ a steady averaged force to determine flow response. Even when unsteady force variation is available as above, the computational expense, associated principally with the far smaller time-step-size required to resolve each actuator period, makes it attractive to employ a time-averaged force to determine response. Such an approach does not resolve the acoustic phenomena, but the observation of relatively small variation in velocity within the actuator cycle, Fig.7d, suggests that many key features may be accurately computed with an averaged force. For practical reasons therefore, in this section the averaged response to the unsteady force (§IV.A.3) is compared with that obtained with the steady average force, Fig.5w, due to the actuator.

The asymptotic response of the flow to the constant averaged force is unsteady, because of the manifestation of separation near the trailing edge and subsequent shedding. Consequently the time-mean response is described in Fig.9 which depicts the velocity, pressure and vorticity fields obtained by averaging the flow over several characteristic times after an asymptotic state is reached. Comparison of each quantity in Fig.8 and Fig.9 indicates that the mean response is very similar suggesting that the detailed unsteady characteristics of the body force are not critical in determining the mean features of the response. A more quantitative comparison of the two forcing approaches is shown in Fig.10. The surface pressure coefficient, Fig.10a, shows a sharp peak near the point of application of the actuator, but relaxes to values typical of the suction pressure. Figure 10b and c compare averaged u-velocity profiles at several different streamwise locations. In the immediate vicinity of the actuator, $X \sim 0.03$, a small negative flow region is evident very near the surface, while a wall jet with peak u-velocity of about 3 occurs in the outer region. Both forcing approaches show the evolution of the wall jet, and the subsequent development of a velocity deficit downstream of the trailing edge and its subsequent diffusion in the wake, where note that the vertical scale has been significantly expanded. Figure 10 thus reiterates the similar mean response obtained from the time-accurate and averaged force fields inside the flow and on the surface. Differences observed in the velocities are modest. For example, at the trailing edge, the peak discrepancy is less than 5%.

This analysis also provides insight into the strengths and limitations of the technique typically employed in phenomenological approaches. The various models explored in Ref. 23 assume a triangular force distribution within which different orientations were chosen. Fields with significant streamwise components were found to be most effective with steady asymptotes while body normal (towards the surface) components also yielded attached flows in the mean. None of the chosen distributions has the complex features obtained with the first-principles approach (Fig.5). Nevertheless, the predominant components are streamwise and towards the surface, with relatively smaller components upstream and away from the surface. Another point of difference has its basis in the observation that for the same value of D_c, at most points in the cycle the force amplitude is smaller than that with the phenomenological approach. Despite these differences, the response is therefore relatively similar, suggesting that while quantitative accuracy and acoustic analysis demands first-principles simulations, a broad preliminary indication of flow sensitivity to applied body force can be conveniently obtained through the phenomenological model.

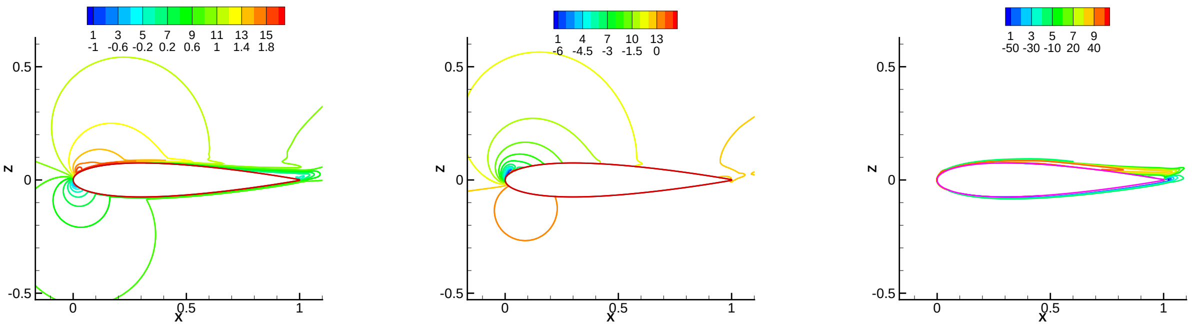

a) u **b)** C_p **c)** ω_y

Figure 9. Mean response of flow to averaged force

5. *Effect of force during negative stroke*

The relative impact of different phase ranges of each individual cycle of the actuator excitation has been subject of scrutiny. Reference 11 for example divides the cycle into “negative-going” and “positive-going” segments depending on the slope of the voltage. The force field described in Fig.5 suggests another natural demarkation into ranges depending on the sign of the voltage. In particular, the effect of the “negative” segment in the phase range $\pi < \phi < 2\pi$ is of interest, since the body force exhibits a significant upstream component in addition to the body normal component.

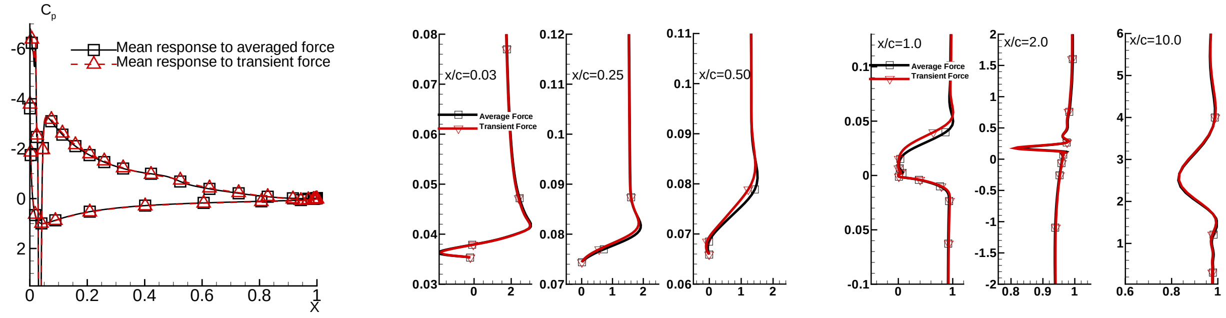

a) C_p **b)** u on upper surface **c)** u at t.e and downstream

Figure 10. Comparison of mean response of flow to time-accurate versus averaged force field

Results averaged after an asymptotic state is reached, are shown in Fig.11 for force fields in which the negative stroke is damped to varying extents. In Fig.11a, results with the original model are displayed while in Figs.11b and c the reverse stroke is damped to 50% and 10% respectively. Although the effect of reducing the reverse stroke to half its normal value is not significant, the near complete elimination results in a significant degradation of control effectiveness. In this case, mean separation occurs at $x/c \sim 0.13$, and the displacement effect of separation increases sharply. The separated shear layer then exhibits vortical structure formation similar to that shown in Fig.3. In addition to the upstream component, the negative stroke is also characterized by a downwards (toward the surface) component. These results suggest that in the absence of turbulence, this latter component during the reverse stroke is an important element of the control effectiveness.

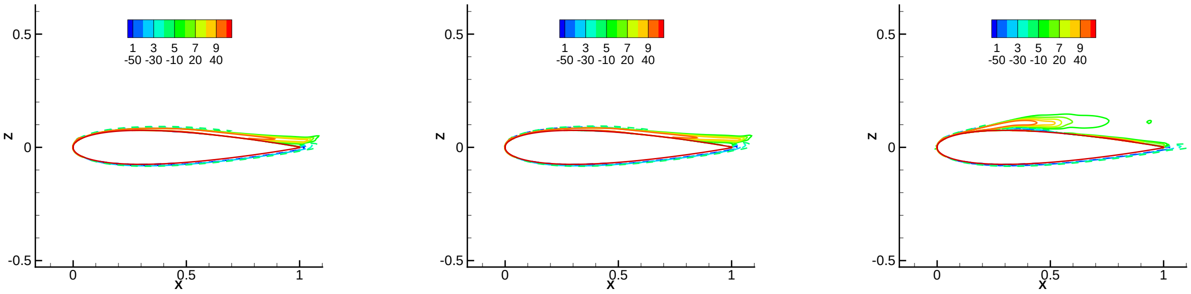

a) No damping **b)** Negative stroke damped 50% **c)** Negative stroke damped 90%

Figure 11. Effect of damping negative stroke on mean ω_y

B. Effect of Reynolds number on control

All calculations described above, as well as those in Ref. 23, utilized a Reynolds number of $45,000$ and $\alpha_a = 15^o$. In order to examine the effect of Reynolds number on control, simulations were performed at $Re = 90,000$ and α_a values of 15^o and 18^o respectively. In the absence of control, the results described below show that the 3-D turbulence structure is crucial in determining the flow field: for example, at $Re = 90,000$, $alpha_a = 15^o$, the 2-D simulations indicate laminar separation and formation of large vortical structures, while the 3-D flow is turbulent and attached. These calculations are thus performed in full 3-D (direct numerical simulations). However, when control is applied, the expense of the first-principles coupling described above becomes prohibitive because of the small time-step-size required to resolve each cycle. To alleviate this situation, the phenomenological approach of Refs. 13, 23 is employed to obtain the body force – this also facilitates comparison with $Re = 45,000$ results of Ref. 23. The results presented earlier suggest that the key aspects of the response, including the development of the wall-jet and attachment process, are similar with phenomenological and first-principles approaches.

1. *Flowfield at $Re = 90,000$, $\alpha_a = 15^o$ - No control*

No-control results at the higher Reynolds number are shown in Fig.12 in terms of instantaneous velocity (Fig. 12a), vorticity contours (Fig. 12b) and pressure (Fig. 12c) contours on the mid-span plane. Mean velocity and vorticity contours are presented in Fig.13a and b, while the mean surface pressure profile is compared with that at $Re = 45,000$

in Fig. 13c. These results indicate that the flow becomes turbulent very quickly downstream of the leading edge, and remains attached in the mean. Several conclusions are readily made by comparing with Fig.2, which displays flow features at $Re = 45,000$. The shear layer emanating from the separation point at lower Reynolds number is absent as is the large separated region beneath it. The surface pressure profile variation, Fig.13c, shows the classic flat shape at the stalled lower Reynolds number case, while the attached flow obtained at higher Reynolds number is yields a characteristic suction profile, with a higher suction peak.

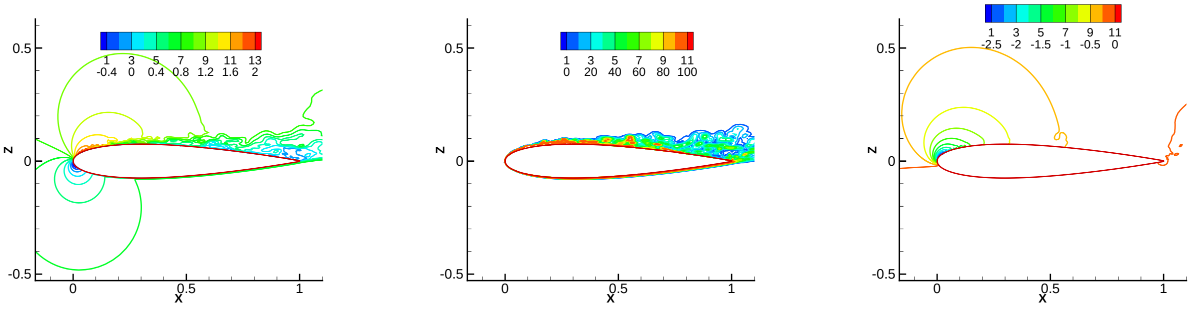

a) u-velocity **b)** $|\omega|$ **c)** p

Figure 12. Instantaneous flow field features at $Re = 90,000$ without control

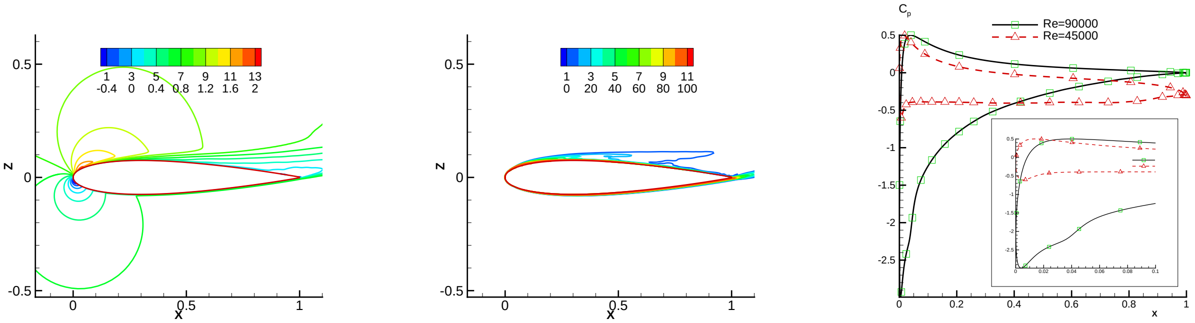

a) u-velocity **b)** vorticity **c)** Surface pressure

Figure 13. Mean flow field features at $Re = 90,000, \alpha_a = 15^o$ without control

2. *Brief description of phenomenological force*

The effect of the actuator on the flow was examined with the phenomenological force model described in Ref. 23. The particular variant denoted "Case 2" is employed. In this, the body force is obtained from

$$\vec{F} = D_c \theta \Delta t \alpha \rho_c \vec{E} \delta \tag{10}$$

where θ is the frequency of the applied voltage, Δt is an effective duty cycle to recover a mean force, α is a factor for collision efficiency, ρ_c is the charge density, $\vec{E}$ is the electric field vector and δ constrains the region of force as below. The charge density is assumed to be uniform in the region of interest. The variation in electric field is approximated through several assumptions. The magnitude is assumed to vary linearly in x and z measured from the actuator position, $|E| = E_o - k_1 x - k_2 z$. The peak value ($E_o = V/d$, where V is the applied voltage and d is the streamwise distance between the two electrodes) occurs at the origin. A further assumption is made that the field value is at or above breakdown level (E_b) in the plasma region, so that $\delta = 1$ when $|E| > E_b$ and $\delta = 0$ otherwise. By choosing the streamwise and body normal extents (b_d and a_d respectively), the values of $k_1 = (E_o - E_b)/b_d$ and $k_2 = (E_o - E_b)/a_d$ are determined. In the frame of reference of the device, $\vec{E}$ is then obtained from:

$$\vec{E} = \frac{|E|}{\sqrt{k_1^2 + k_2^2}} \left\{ \kappa_\xi k_2 \hat{\xi} + \kappa_\eta k_1 \hat{\eta} \right\} \tag{11}$$

Here, $\hat{\xi}$ and $\hat{\eta}$ are unit vectors aligned respectively along and normal to the exposed electrode, which is assumed to lie flush on the surface of the body. For the airfoil, this coordinate system is located at the tangent to the surface at the leading edge of the electrode. In all cases, a single actuator is assumed, though its location and strength are varied. The body force orientation is adjusted by choosing κ_ξ and κ_η. In this case, values of 1 and -1 respectively were employed (vertical force component points towards the surface). The values of $\theta = 3000$, $\Delta t = 67\mu s$, $\alpha = 1$, $\rho_c = 10^{11}/cm^3$ are taken from Ref. 13. The nominal values chosen for the parameters describing strength and extent are $D_c = 2400$ (same as employed in the results of § IV.A), $a_d = 0.018$ are $b_d = 0.024$, where a and b are normalized by chord length. The force field obtained when the actuator is placed near the leading edge with origin at $X_o = 0.028$, $Z_o = 0.034$, is shown in Fig.14a at the mid-span location. The force has no gradients in the spanwise direction.

3. *Effect of actuator on flow at* $Re = 90,000$, $\alpha_a = 15^o$

Even though the flow is attached, it is illustrative to examine the effect of control because of its implication from the standpoint of laminarization techniques as well as off-design performance. To this end, the actuator was positioned separately at two locations: the first near the leading edge as above, and the second at mid-chord. Results obtained with the first actuator location are shown in Fig.14b through d. Over most of the wing section, the flow becomes attached and laminar. The wall-jet is a prominent feature as before - instantaneous and mean results are therefore similar with the exception of the region downstream of the trailing edge where the shear layer becomes unstable. Fig. 14c compares u-velocity profiles at mid-chord without and with control for the two Reynolds numbers examined. Without control, the flow is stalled at $Re = 45,000$ and the mean u-velocity is negative. At $Re = 90,000$, the velocity profile is typical of turbulent attached flow with a boundary layer height of 5% chord. With control on, the existence of the wall-jet yields a peak velocity exceeding $2U_\infty$ and a wall velocity gradient higher than the no-control turbulent flow. The peak is slightly larger for $Re = 45,000$ and for both cases u relaxes to $u_\infty = U_\infty \cos(15^o)$ in the far field. Comparison of surface C_p at $Re = 90,000$ with and without control, Fig.14d, indicates that the effect of the actuator is relatively small, with a modest reduction of pressure over much of the upper surface and a small spike near the point of application of the actuator. For this actuator location, the main impact of control is to replace a turbulent attached boundary layer with a laminar attached wall-jet.

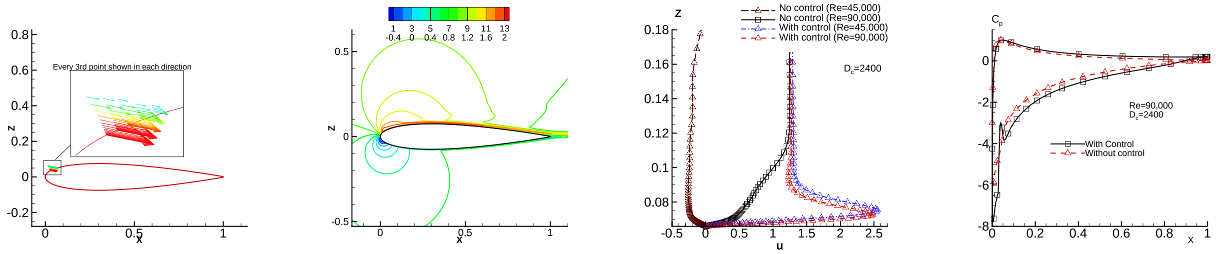

a) Force **b)** Mean u-velocity **c)** u profiles at mid-chord **d)** C_p profiles

Figure 14. Effect of actuator located near leading edge on flow at $Re = 90,000$

The two prominent fluid dynamic effects, turbulence and separation, can be coupled to actuator positioning and orientation to yield several different phenomena. In Ref. 32, a "backward"-oriented actuator, *i.e.*, where the actuator is placed so that the embedded electrode is upstream of the exposed electrode and the body force points predominantly against the flow, is employed to induce attachment by triggering turbulence in a separated flow. In an analogous fashion, the "forward" facing actuator employed above may be deployed to trigger separation by suitable placement in a turbulent flow by laminarizing parts of the flow field. To demonstrate this, the actuator in the previous case was moved from near the leading edge to the point of maximum thickness in the turbulent attached flow, as depicted in Fig.15a. Instantaneous velocity and vorticity magnitude contours are plotted in Fig.15b and c respectively after an asymptotic state is reached. Comparison with the baseline flow presented earlier in Fig.12 indicates that the actuator has triggered separation near the leading edge: in fact gross manifestations of separation appear shortly after the actuator is turned on. The flow field takes on the character of the no-control lower Reynolds case in other aspects as well: the instantaneous vorticity contours of Fig. 15c display a trailing edge vortical structure that resembles that observed at $Re = 45,000$ (see Ref. 23). These results are significant in several respects. They demonstrate the potential for global actuator impact and highlight the need to consider off-design performance. The dynamics indicate further that inviscid or 2-D simulation procedures are unsuitable for such studies.

4. *Control of separated flow at high Reynolds number,* $Re = 90,000$, $\alpha_a = 18^o$

As noted earlier, increasing the Reynolds number from $45,000$ to $90,000$ at an angle of attack of 15^o results in a turbulent attached flow. In order to examine the effect of actuation in a separated higher Reynolds number flow, the

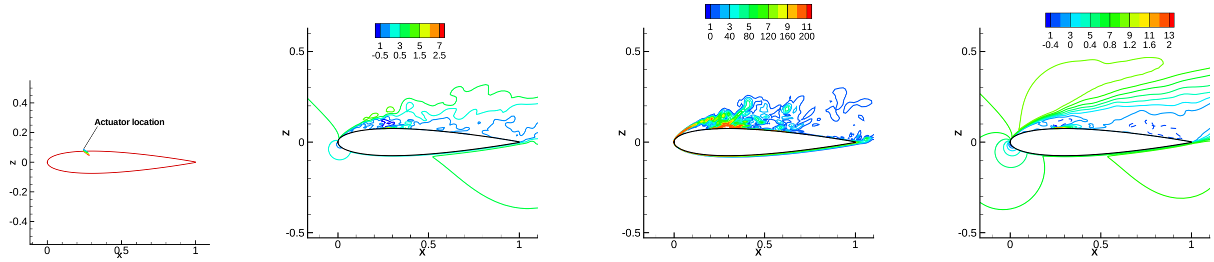

a) Force location **b)** Instantaneous u **c)** Instantaneous $|\omega|$ **d)** Mean u

Figure 15. Effect of actuator located at maximum thickness location at $Re = 90,000$**,** $\alpha_a = 15^o$

angle of attack was increased to 18^o. The main features of the flow without control are shown in Fig.16. The effect of angle-of-attack may be discerned by comparison with Fig. 12, which shows results at the same Reynolds number and $\alpha_a = 15^o$. The instantaneous u-velocity and vorticity indicate that the flow is turbulent over the upper surface of the wing section, while the time-averaged velocity, Fig. 16c shows that separation occurs at about $x/c \sim 0.5$.

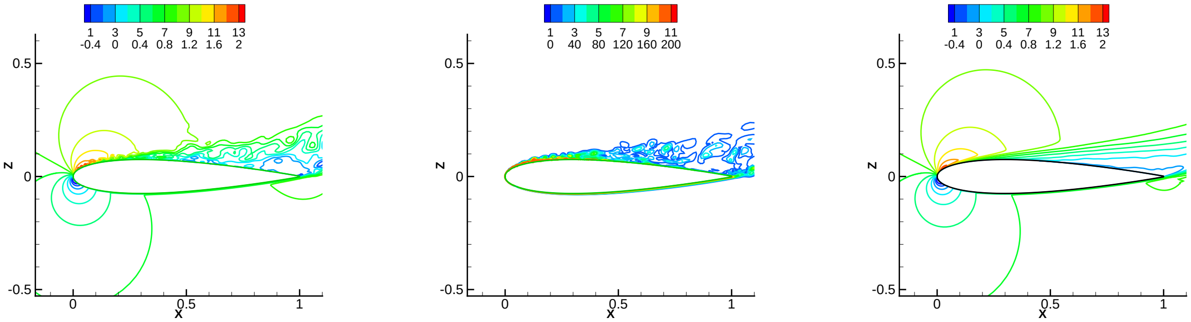

a) Instantaneous u **b)** Instantaneous $|\omega|$ **c)** Mean u

Figure 16. Flow features at $Re = 90,000, \alpha_a = 18^o$ **(no control)**

The effect of control on this separated flow, with the actuator placed near the leading edge, is shown in Fig. 17. In the initial transients (not shown), the wall jet is established over the entire wing surface. This "impulse" effect, discussed in Ref. 23, is short lived however, as instabilities arise in the shear layer downstream of the trailing edge. These disturbances subsequently propagate upstream and yield a turbulent boundary layer over the wing as shown with instantaneous u-velocity contours in Fig. 17a . The mean u-velocity contours, Fig. 17b show the wall jet as a clear feature until $X \sim 0.8$, beyond which turbulent diffusion yields a thicker disturbed region but with lower peak velocities. Figure 17c exhibits the mean velocity profiles at the mid-chord for three cases in which the Reynolds number and angle-of-attack are varied independently but with the same coefficient $D_c = 2400$. All cases exhibit the wall-jet structure, and, since D_c scales the electric with the inertial force, peak velocities in the jet are similar, reaching about $2.5U_\infty$. The principal differences are observed in the near-wall profile fullness which is highest in the high-Reynolds number and angle-of-attack case and the wall-jet remains turbulent.

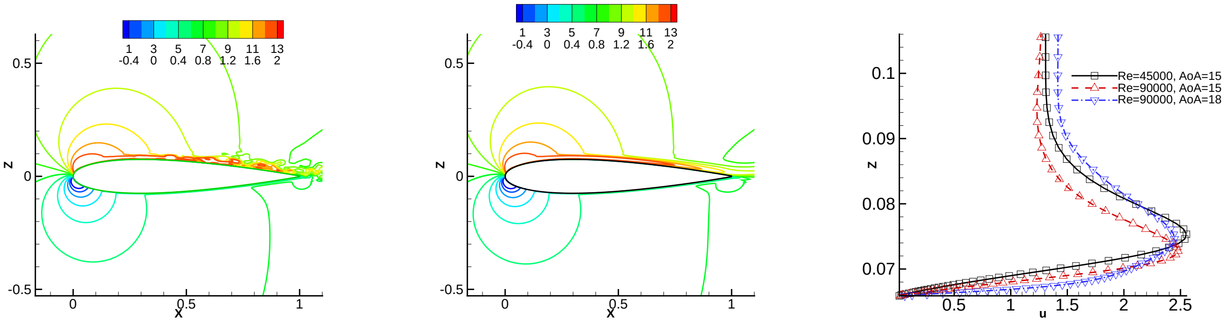

a) Instantaneous u **b)** Mean u **c)** u-profiles at mid-chord

Figure 17. Effect of control with actuator located near leading edge at $\alpha_a = 18^o$ **and** $Re = 90,000$

5. *Effect of actuator strength*

The effect of actuator strength on the flow field is examined for $Re = 90,000$ and angle-of-attack of 18^o by reducing D_c from 2400 for the previous cases to half that. Results shown in Fig. 18 indicate that there is no significant qualitative impact associated with the reduction. The instantaneous u-velocity shows that the boundary layer remains turbulent, similar to the situation depicted in Fig. 17a. Further, the mean velocity, Fig.18b indicates that the flow remains attached though the prominence of the wall-jet is clearly diminished when D_c is lowered. Although not shown, each turbulent attached flow exhibits similar surface C_p profiles. The quantitative differences are displayed in the velocity profiles at mid-chord, shown in Fig.18c. The lower forcing yields a wall-jet with a significantly smaller peak velocity $1.5U_\infty$ versus $2.5U_\infty$. These results suggest that the effect of turbulence in establishing attachment augments that of the development of a wall-jet.

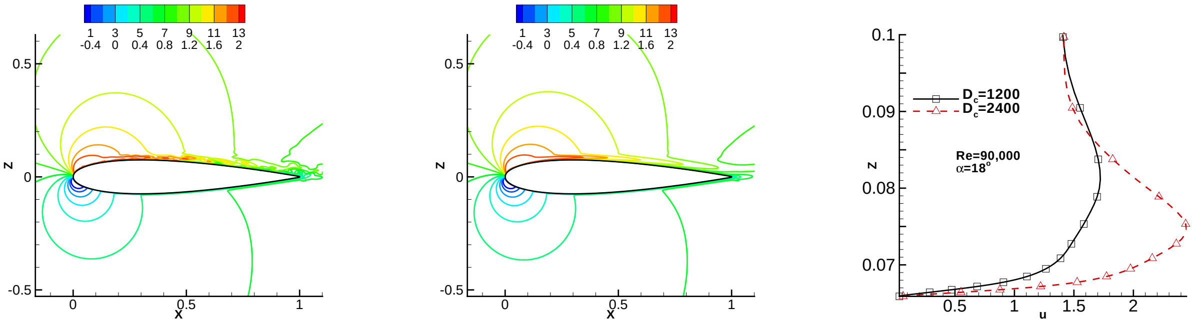

a) Instantaneous u-velocity **b)** Mean u-velocity **c)** Comparison of u-profiles

Figure 18. Effect of actuator strength at angle-of-attack 18^o and $Re = 90,000$

C. Effect of Duty Cycle

Duty cycles, in which the actuator is switched on intermittently in a usually regular pattern, have been explored to enhance effectiveness in the context of dielectric barrier discharges either to reduce power requirement or to influence fluid dynamic instabilities to accomplish specific goals.[10] For the wing section, both objectives can be achieved through the combined effects of optimizing near wall momentum injection and triggering of transition to turbulence. To examine these phenomena, the phenomenological force model was employed for the stalled $Re = 45,000, \theta = 15^o$ condition with two different inter-pulse periods, $T_p = 0.7T_c$ and $T_p = 0.25T_c$, of same duty cycle (20%) and power requirement. The first value $0.7T_c$ represents the time required for perceptible manifestation of separation to appear after cessation of the body force in a fully attached situation (see Ref. 23 for transient effects after the actuator is switched off). Results obtained with this forcing suggest exploration with the lower value. The amplitude of the imposed force for the $T_p = 0.7T_c$ case is shown in Fig. 19 as a function of time.With duty cycle of 20%, the actuator is on for $0.14T_c$ in each cycle. The start and end of the on-period is smoothed with a fifth order polynomial:

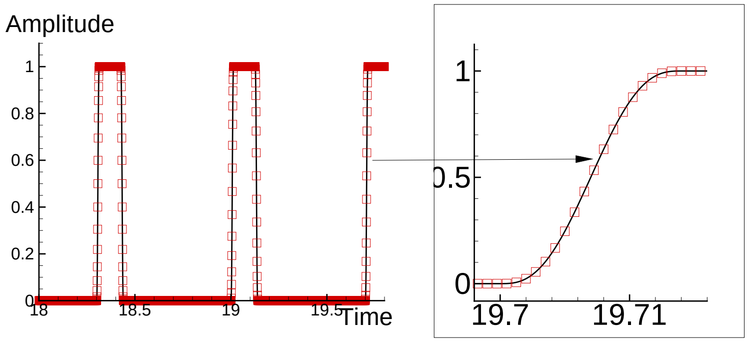

Figure 19. Amplitude variation in duty cycle, $T_p = 0.7T_c$

$$A(t) = at^5 + bt^4 + ct^3 + dt^2 + et + f \tag{12}$$

For the ramp-up segment, say between t_1 and t_2, the coefficients are obtained by enforcing $A(t_1) = 0$, $A(t_2) = 1$ and $\partial A/\partial t = 0$ and $\partial^2 A/\partial t^2 = 0$ at t_1 and t_2:

$$\begin{array}{llll} a = -\frac{6}{D} & b = \frac{15(t_1+t_2)}{D} & c = \frac{-10\left(t_1^2+4t_1t_2+t_2^2\right)}{D} & \\ d = \frac{30t_1t_2(t_1+t_2)}{D} & e = -\frac{30t_1^2t_2^2}{D} & f = \frac{t_1^3\left(t_1^2-5t_1t_2+10t_2^2\right)}{D} & D = (t_1-t_2)^5 \end{array} \tag{13}$$

10% of the duty cycle is employed for ramp-up and ramp-down (*i.e.*, $0.014T_c$ for $T_p = 0.7T_c$ and 0.005 for $T_p = 0.25T_c$).

The response may be naturally divided into two time ranges: the initial transients and the asymptotic state. The former are shown for $T_p = 0.7T_c$ in Fig. 20 which depicts instantaneous u contours at selected points in the first cycle, with time being measured from the onset of control. The initial condition, Fig. 20a, corresponds to an instantaneous pattern of the separated flow with a shear layer that rapidly becomes turbulent. The onset of the body force interrupts the formation of the shear layer, together with the eruption of a sequence of vortical structures, similar to those described in Ref. 32. By the time instant of Fig. 20c, the force has been switched off. Subsequently, the initial structures in the disturbed region are essentially convected downstream without the sustaining effect of the vortex sheet. At the end of the interpulse period, incipient separation is evident near the leading edge, but its development is inhibited by the onset of the next actuation cycle.

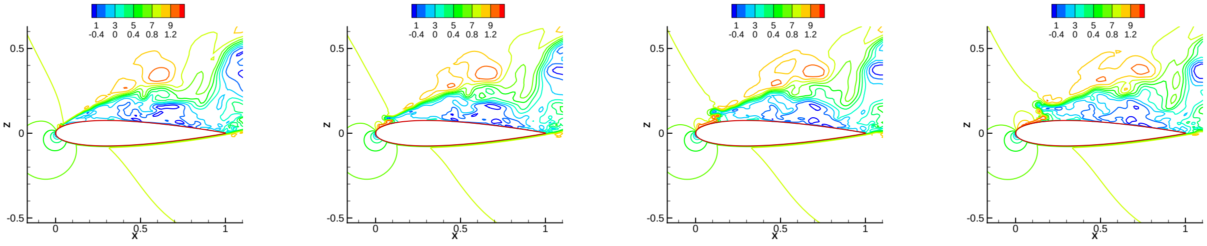

a) $T = 0.0125T_c$ **b)** $T = 0.0625T_c$ **c)** $T = 0.1125T_c$ **d)** $T = 0.1625T_c$

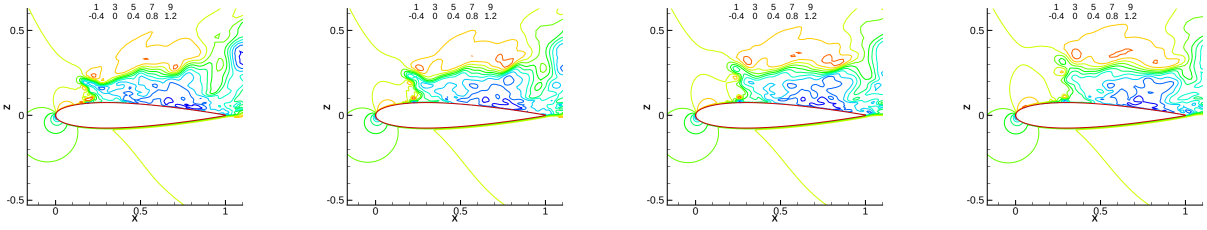

e) $T = 0.2125T_c$ **f)** $T = 0.2625T_c$ **g)** $T = 0.3125T_c$ **h)** $T = 0.3625T_c$

Figure 20. Initial transients after actuation with 20% duty cycle and interpulse period $0.7T_c$. Time measured after onset of actuation.

The sequence of events when the asymptotic state is reached is shown in Fig.21. Figure 21a depicts the situation at roughly the mid-point of the off segment of the cycle. A major feature in each figure is the existence of relatively large coherent structures outside of the near wall jet region which are convected. This is observed to be the direct result of the impulsive nature of the forcing. Upon switching on the actuator a set of vortices is initiated which lift from the surface of the wing. In the figures, two such structures arising during successive on-phases of the actuator have been identified as A and B respectively. These structures diffuse as they are convected downstream, partly as a consequence of the coarser mesh, but maintain their overall form and can be identified even near the trailing edge. By frame (e), separation inception is apparent near the leading edge, becoming prominent by frame (f). In frames (g) and (h), the actuator is on, injecting momentum near the surface and initiating the formation of a new local jet preceeded by the vortex pair B, which follows the same development as A, thus repeating the sequence.

The development of incipient separation in the previous simulations suggests that the interpulse period of $0.7T_c$ be reduced. To explore the effect of shorter bursts of more frequent actuation, a simulation was conducted at $T_p = 0.25T_c$. With the same duty cycle and ramp-up and ramp-down times (as a ratio of the duty cycle) the power requirements remain the same. Results are shown in Fig.22 after a periodic asymptote is reached. Note that the time elapsed between frames is now considerably shorter compared to that in Fig. 21. The flow downstream and near the surface is more disturbed than in the longer cycle. The results show that the eruption of vortical structures persists in this case. Close scrutiny indicates that up to three distinct vortex pairs of varying strength - the leading pair being the most distinct - are generated with each actuator onset event. Overall, the size of these structures is smaller than in the previous case and their trajectory remains relatively closer to the surface.

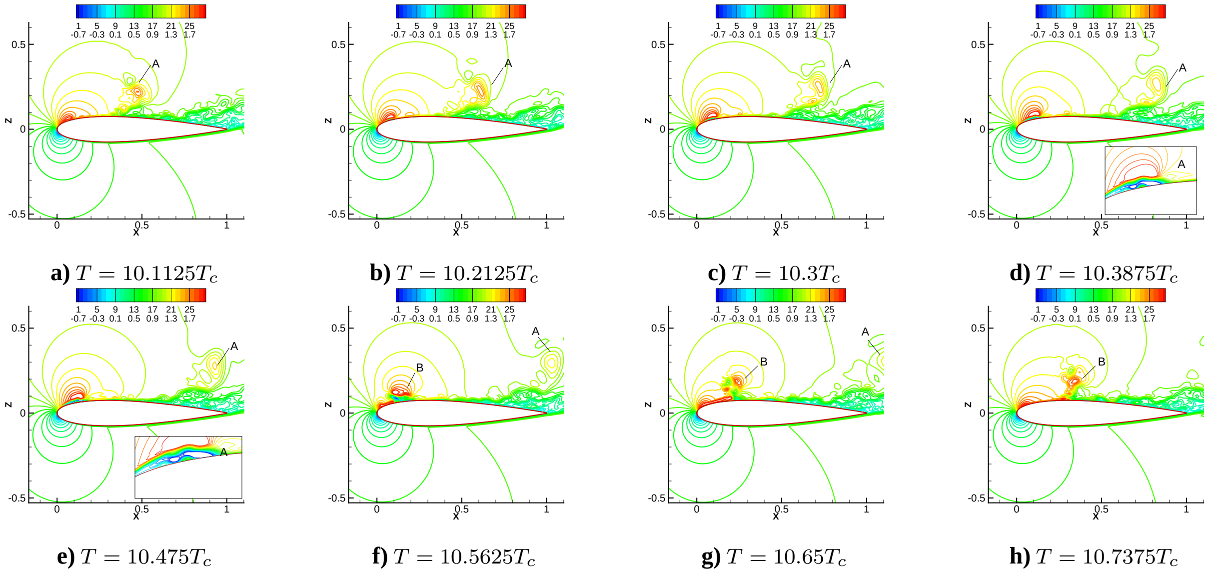

a) $T = 10.1125T_c$ **b)** $T = 10.2125T_c$ **c)** $T = 10.3T_c$ **d)** $T = 10.3875T_c$

e) $T = 10.475T_c$ **f)** $T = 10.5625T_c$ **g)** $T = 10.65T_c$ **h)** $T = 10.7375T_c$

Figure 21. Asymptotic response with 20% duty cycle of interpulse period of $0.7T_c$

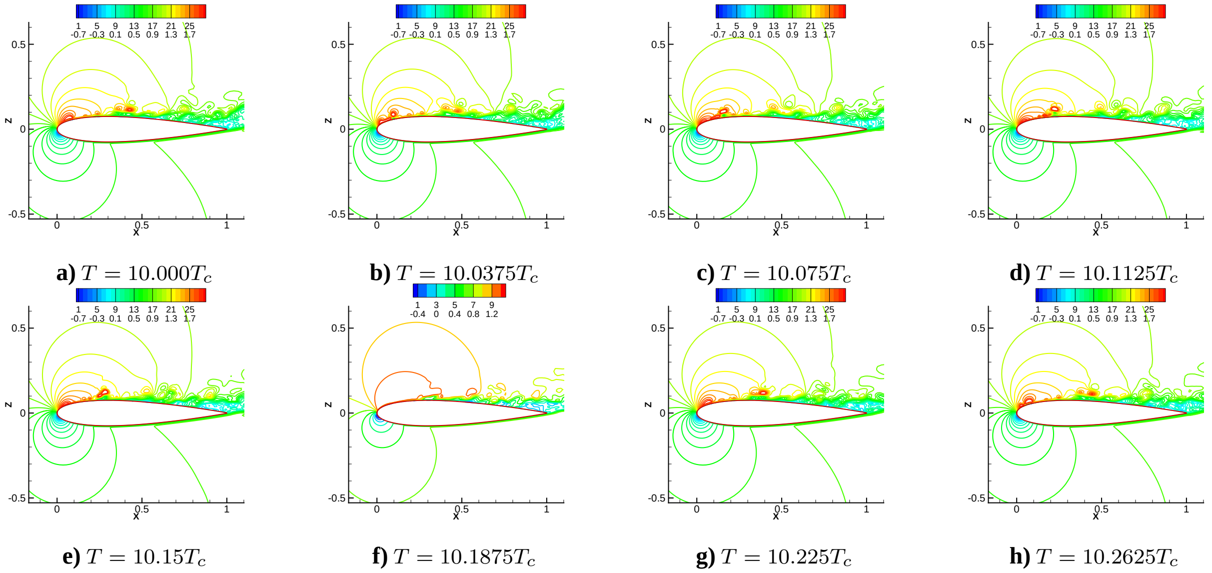

a) $T = 10.000T_c$ **b)** $T = 10.0375T_c$ **c)** $T = 10.075T_c$ **d)** $T = 10.1125T_c$

e) $T = 10.15T_c$ **f)** $T = 10.1875T_c$ **g)** $T = 10.225T_c$ **h)** $T = 10.2625T_c$

Figure 22. Asymptotic response with 20% duty cycle of interpulse period of $0.25T_c$: u-velocity

The time-averaged response to actuation with the two interpulse periods is shown in Fig. 23. Figures 23a and b, depict the u-velocity after an asymptotic state is reached. The development of the initial stages of separation for the longer interpulse period case is reflected in a bulging of the boundary layer near the leading edge (see inset) and the boundary layer displays rapid growth aft of the mid-chord region because of turbulence. The mean flow remains attached over the upper surface. In contrast, the smaller interpulse period case exhibits separation in the mid-chord region but the smaller boundary layer height near the trailing edge reflects the closer proximity of the vortical structures to the wing surface. Mean velocity profiles are compared at mid-chord and one chord-length downstream of the trailing edge in Fig. 23c. At mid-chord, the shorter interpulse period yields a shallower velocity profile but a sharper and higher peak ($u/U_\infty \sim 1.4$), while the larger period case exhibits a more diffuse distribution. However, these differences are mitigated downstream, where similar velocity defects are observed in the wake. Mean C_p profiles plotted in Fig. 23d indicate that with the exception of the region in the immediate vicinity of the actuator, the mean pressure fields are similar with the two different interpulse periods.

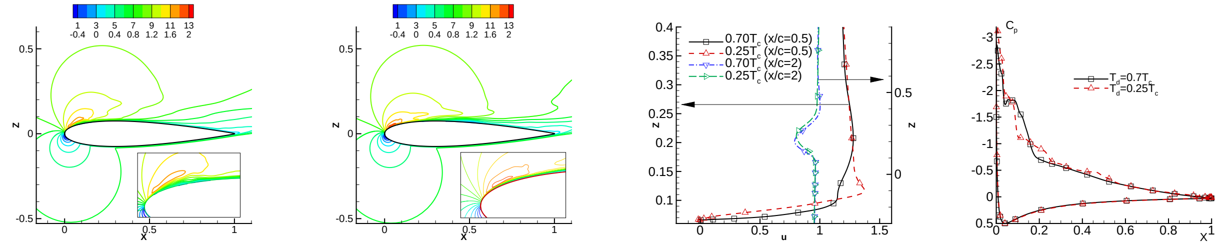

a) Mean u-velocity for $T_p = 0.7T_c$

b) Mean u-velocity for $T_p = 0.25T_c$

c) Mean u profiles

d) C_p profiles

Figure 23. Effect of interpulse period variation

V. Conclusions

Full Navier-Stokes simulations are reported on plasma-based flow control of a stalled NACA 0015 wing section at Reynolds numbers of $45,000$ and $90,000$ and angles of attack 15^o and 18^o. The time-accurate force field obtained from a self-consistent simulation at $5kHz$ and $2kV$ rms is suitably scaled and employed to determine the response of the flow. The unsteady asymptotic pattern as well as the mean flow are described in terms of the small-scale structures, acoustic signals and the development of a wall-jet. Separation location moves downstream with perceptible detachment occurring at 80% chord. In many key respects, the time-averaged flowfield is similar to that obtained from a steady time-averaged force and that reported with a phenomenological model in an earlier publication, though more investigation is warranted.

This simpler averaged model is employed with 3-D direct numerical simulations to deduce Reynolds number, force scaling and duty cycle effects. At higher Reynolds number, $90,000$, the no-control flow at 15^o angle-of-attack becomes turbulent immediately downstream of the leading edge and remains attached in the mean. The actuator laminarizes the flow with the formation of a wall-jet. When the actuator location is moved to the point of maximum airfoil thickness, the flow near the leading edge becomes laminar and separates. To explore stall control at $Re = 90,000$, the angle of attack was raised to 18^o. Actuation at the leading edge recovers the attached laminar wall jet on the upper surface. The effect of actuator force strength on the response is examined and the combined effects of the laminar wall jet and subsequent turbulence breakdown are described. Finally, the effect of pulsing is documented at Reynolds number $45,000$ with 20% duty cycle and interpulse periods of 0.7 and 0.25 characteristic times respectively.

A. ACKNOWLEDGMENTS The authors are grateful for AFOSR sponsorship under tasks monitored by Drs. J. Schmisseur, F. Fahroo and R. Jefferies. This work was also supported by a grant of computational time from the DoD HPC Shared Resource Centers at NAVO, AHPCRC, ASC and ERDC.

References

[1] Roth, J., Sin, H., R.C.M., M., and Wilkinson, S., "Flow Re-attachment and Acceleration by Paraelectric and Peristaltic Electrohydrodynamic Effects," *AIAA Paper 2003-531*, Jan. 2003.

[2] Enloe, C., McLaughlin, T., Van Dyken, R., Kachner, K., Jumper, E., Corke, T., Post, M., and Haddad, O., "Mechanisms and Responses of a Single Dielectric Barrier Plasma Actuator: Geometric Effects," *AIAA J.*, Vol. 42, No. 3, 2004, pp. 595–604.

[3] Post, M. and Corke, T., "Separation Control on High Angle of Attack Airfoil Using Plasma Actuators," *AIAA Paper 2003-1024*, 2003.

[4] Corke, T., Jumper, E., Post, M., Orlov, D., and McLaughlin, T., "Application of Weakly-Ionized Plasmas as Wing Flow-Control Devices," *AIAA Paper 2002-0350*, Jan. 2002.

[5] Post, M. and Corke, T., "Separation Control Using Plasma Actuators - Dynamic Stall Control on an Oscillating Airfoil," *AIAA Paper 2004-2517*, June 2004.

[6] Opaits, D., Roupassov, D., Starikovskaia, S., Starikovskii, A., Zavialov, I., and Saddoughi, S., "Plasma Control of Boundary Layer Using Low-Temperature Non-Equilibrium Plasma of Gas Discharge," *AIAA Paper 2005-1180*, Jan. 2005.

[7] Jacob, J., Rivir, R., Carter, C., and Estevadeordal, J., "Boundary Layer Flow Control Using AC Discharge Plasma Actuators," *AIAA Paper 2004-2128*, June 2004.

[8] Jacob, J., Ramakumar, K., Anthony, R., and Rivir, R., "Control of Laminar and Turbulent Shear Flows Using Plasma Actuators," *Fourth Int. Symp on Turbulence and Shear Flow Phenomena*, , No. TSFP4-225, June 2005.

[9] Hultgren, L. and Ashpis, D., "Demonstration of Separation Delay with Glow-Discharge Plasma Actuators," *AIAA Paper 2003-1025*, 2003.

[10] Corke, T. and Post, M., "Overview of Plasma Flow Control: Concepts, Optimization and Applications," *AIAA Paper 2005-0563*, 2005.

[11] Baird, C., Enloe, C., McLaughlin, T., and Baughn, J., "Acoustic testing of the dielectric barrier discharge (DBD) plasma actuator," *AIAA Paper 2005-0565*, Jan 2005.

[12] Roth, J., "Aerodynamic flow acceleration using paraelectric and peristaltic electrohydrodynamic (EHD) effects of a One Atmosphere Uniform Glow Discharge Plasma (OAUGDP)," *Phys. Plasmas*, Vol. 10, 2003, pp. 2117.

[13] Shyy, W., Jayaraman, B., and Andersson, A., “Modeling of Glow-Discharge Induced Fluid Dynamics,” *J. Appl. Phys.*, Vol. 92, 2002, pp. 6434.

[14] Voikov, V., Corke, T., and Haddad, O., “Numerical simulation of flow control over airfoils using plasma actuators,” *Bulletin of the APS*, 2004.

[15] Boeuf, J. and Pitchford, L., “Two-Dimensional Model of a Capacitively Coupled RF Discharge and comparisons with experiments in the Gaseous Electronics Conference Reference Reactor,” *Phys Ref*, Vol. E 51, 1995, pp. 1376.

[16] Surzhikov, S. and Shang, J., “Multi-Fluid Model of Weakly Ionized Electro-Negative Gas,” *AIAA Paper 2004-2659*, June 2004.

[17] Poggie, J., “Numerical Exploration of Flow Control with Glow Discharges,” *AIAA Paper 2004-2658*, June 2004.

[18] Hilbun, W. and Case, B., “Preliminary Development of a Computational Model of a Dielectric Barrier Discharge,” *AIAA Paper 2005-1176*, Jan 2005.

[19] Roy, S. and Gaitonde, D., “Radio frequency induced ionized collisional flow model for application at atmospheric pressures,” *J. Appl Phys*, Vol. 96, 2004, pp. 2476–2481.

[20] Roy, S. and Gaitonde, D., “Modeling Surface Discharge Effects of Atmospheric RF on Gas Flow Control,” *AIAA Paper 2005-0160*, Jan 2005.

[21] Roy, S. and Gaitonde, D., “Multidimensional Collisional Dielectric Barrier Discharge for Flow Control at Atmospheric Pressures,” *AIAA Paper 2005-4631*, 2005.

[22] Roy, S., Singh, K., Kumar, H., Gaitonde, D., and Visbal, M., “Effective Discharge Dynamics for Plasma Flow Control,” *AIAA Paper 2006-0374*, 2006.

[23] Gaitonde, D., Visbal, M., and Roy, S., “Control of Flow Past a Wing Section with Plasma-based Body Forces,” *AIAA Paper 2005-5302*, 2005.

[24] Lele, S., “Compact Finite Difference Schemes with Spectral-like Resolution,” *Journal of Computational Physics*, Vol. 103, 1992, pp. 16–42.

[25] Visbal, M. and Gaitonde, D., “High-Order Accurate Methods for Complex Unsteady Subsonic Flows,” *AIAA Journal*, Vol. 37, No. 10, 1999, pp. 1231–1239.

[26] Gaitonde, D., Shang, J., and Young, J., “Practical Aspects of Higher-Order Numerical Schemes for Wave Propagation Phenomena,” *Int. Jnl. for Num. Methods in Eng.*, Vol. 45, 1999, pp. 1849–1869.

[27] Gaitonde, D. and Visbal, M., “Pade-type Higher-Order Boundary Filters for the Navier-Stokes Equations,” *AIAA J.*, Vol. 38, No. 11, Nov. 2000, pp. 2103–2112.

[28] Ward, L., “Calculations of Cathode-Fall Charactristics,” *Journal of Applied Physics*, Vol. 33, No. 9, 1962, pp. 2789–2794.

[29] Roy, S., Pandey, B., Poggie, J., and Gaitonde, D., “Modeling low pressure collisional plasma sheath with space-charge effect,” *Physics of Plasmas*, Vol. 10, 2003, pp. 2578–2585.

[30] Balagangadhar, D. and Roy, S., “Design Sensitivity Analysis and Optimization of Steady Fluid-Thermal Systems,” *Computer Methods in Applied Mechanics and Engineering*, Vol. 190, Aug. 2001, pp. 5465–5479.

[31] Roy, S. and Pandey, B., “Development of a Finite Element-Based Hall-Thruster Model,” *J. Prop. Power*, Vol. 19, 2003, pp. 964–975.

[32] Visbal, M. and Gaitonde, D., “Control of Vortical Flows using Simulated Plasma Actuators,” *AIAA Paper 2006-0505*, 2006.